


Evaporation-driven assembly of colloidal nanoparticles into clusters: A dissipative particle dynamics study

Tu Vu-Minh, Anh Dao-Hong, Phuong Bui-Bich , Nam Nguyen-Tran-Thanh, Cuong Tran-Manh, Linh Tran-Phan-Thuy ,
Hien Doan-Thi, Hoang Luc-Huy *, and Hai Pham-Van [†]

Department of Physics, Hanoi National University of Education, 136 Xuanthuy Road, Cau Giay, Hanoi, Vietnam



(Received 17 March 2023; accepted 20 June 2023; published 11 July 2023)

In this work we consider a simulation strategy for assembling Janus nanoparticles in oil-in-water emulsion droplets by evaporation based on the dissipative particle dynamics method. Our simple method reproduces all the observed cluster configurations that have been explored experimentally. In addition, the kinetic process of cluster formation is systematically investigated. We observe a structural transition from spherical packings to minimal second-moment configurations via visual inspection and a simple angle parameter. We reveal that the critical volume at which the transition occurs is a cubic function of the number of particles, N . Our approach also allows us to anticipate higher-order clusters, overcoming the limitations of the standard methods in the literature. Similarly to small N values, we find that for each N in the range of 16–39, all final clusters have a unique configuration.

DOI: [10.1103/PhysRevE.108.014602](https://doi.org/10.1103/PhysRevE.108.014602)

I. INTRODUCTION

Over the past decades, the assembly of colloidal particles into intricate structures has emerged as a new subfield of colloid research [1,2]. Colloidal crystals, resulting from a long-range ordered arrangement of spherical particles, are the most widely studied motifs [3,4]. Recently, besides colloidal crystals, other assemblies of a limited number of identical or dissimilar component particles, termed colloidal clusters, have attracted attention because these clusters may be considered as colloidal analogs to molecules [5–7]. In addition, they have opened up new possibilities to control the optical, electric, and magnetic properties of advanced materials [8].

It is common for research on the adsorption of spherical particles at oil-water interfaces to focus on two types of particles. The first type consists of particles with a homogeneous surface that exhibits uniform wettability. The second type, known as Janus particles, has two surface regions with distinct wettability characteristics. Homogeneous particles are highly surface-active but do not possess amphiphilic properties, while Janus particles are both surface-active and amphiphilic [9].

Water-in-oil and oil-in-water emulsion droplets have provided excellent platforms for preparing colloidal clusters. Velev *et al.* [10] discovered a particularly potential strategy, via evaporation of aqueous droplets, to prepare shells of a large number of homogeneous particles [11]. Colloidal particles adsorbed at the water-oil interface reduce the free energy. During the evaporation process of the droplets, the particles are brought closer together by capillary forces and kept together by van der Waals interactions. Using this method,

Manoharan *et al.* [12] created micron-sized clusters containing several polystyrene spheres, N . Interestingly, this process, which has been carried out with various materials [13,14] or different particle sizes from micro- to nanometers [15–18], produces defined clusters in which all clusters with the same N value are unique. Such cluster structure for $N \leq 11$ corresponds to dense packings that minimize the second moment of mass distribution, M_2 , defined as $M_2 = \sum_{i=1}^N (\mathbf{r}_i - \mathbf{r}_{\text{cm}})^2$, where \mathbf{r}_i is the center of the mass of the i th and \mathbf{r}_{cm} is the center of the mass of the cluster [19]. Larger cluster packings do not minimize M_2 but produce unique clusters with second-moment values near the minimum values. To the best of our knowledge, there have been no experimental investigations exploring the structures of clusters with $N > 15$ specifically assembled through evaporation-driven assembly.

Recent research has attempted to explain the physical principles underlying the formation of cluster configurations. Lauga and Brenner [20] performed a numerical simulation and theoretical calculation of homogeneous particles absorbed at the droplet surface. During slow evaporation, the colloidal particles initially organize themselves to obtain maximum surface density. Specifically, they must be packed in spherical packing when the droplet volume exceeds a critical volume. Spherical packing, also known as the Tammes problem, is to find the arrangement of a certain number of equal circles on a sphere to maximize the smallest distance between them [21,22]. However, when the droplet volume decreases below the critical volume, the interface of the droplet is deformed. As a result, the particles must rearrange themselves [12]. Manoharan *et al.* [12] suggested that the final structure of clusters is a collapsed state of the spherical packing.

Lauga and Brenner [20] indicated that the unique structure of each N -sphere cluster might be predicted by minimizing the total surface free energy during drying. The authors consid-

*hoanglhsp@hnue.edu.vn

[†]haipv@hnue.edu.vn

ered single droplets with various numbers of adsorbed particles. The model accurately reproduced the experimental packings for $9 \leq N \leq 14$ but did not hold for $N = 7$, $N = 8$. Furthermore, the computations required to minimize the continuously changing surface between the colloids were complicated and time consuming. Also, the method seems unsuitable for $N > 15$. Using Monte Carlo simulations, Schwarz *et al.* [18] investigated the cluster formation of colloidal particles on droplet surfaces and found good quantitative agreement between simulation and experimental data for cluster size distribution. Schwarz *et al.* [18] were able to reproduce the cluster structure, which is in agreement with the experiment for $N \leq 12$ except for $N = 11$. However, because the particles were trapped on a continuous and smooth surface, there did not seem to be a pathway for interior spheres to form, in contrast to the experimental data. Peng *et al.* [23] investigated a two-step simulation procedure to predict the cluster structures assembled from dumbbell-shaped particles. In the first stage, the colloidal particles are kept on the surface of a shrinking spherical shell. In the second stage, when the particles stop moving after the long-time self-diffusion and the pressure sharply increases, the minimal condition M_2 is applied. The authors first used the approach on spherical particle clusters with cluster size $4 \leq N \leq 14$ and found that the experimentally observed clusters $N \leq 12$ agree with the simulated clusters after M_2 minimization. For larger clusters ($N > 12$), no apparent match between simulations and experiments can be observed. The current theoretical and simulation methods in the literature are generally suitable experimentally at relatively low N values where the minimum condition M_2 is satisfied. Until now, there are no theoretical or simulation studies to accurately reproduce the cluster structures at $13 \leq N \leq 15$ or to enable the prediction of higher-order cluster structures.

In addition to the extensive studies on the assembly of homogeneous particles, numerous other research works have focused on the equilibrium behavior of Janus particles [24–27], revealing a rich self-assembly behavior leading to various structures such as micelles, vesicles, and lamellar phases. For example, Sciortino *et al.* [28,29] investigated the behavior of the phase diagram when transitioning from a spherical attractive potential to a Janus potential, as well as the collective structure and clustering of a Janus particle system. Rosenthal *et al.* [30] examined the formation of structures in the bulk phase of amphiphilic Janus particles and discovered that below a density-dependent aggregation temperature, the Janus particles in the model self-assemble into a diverse range of cluster types. However, these studies examined the equilibrium behavior of Janus particles without taking into account the assembly process via emulsion droplet evaporation. As a result, the assembled structures they observed differ from those obtained through the emulsion droplet evaporation method.

In the current work, we employ dissipative particle dynamics to study the evaporation-driven assembly of Janus nanoparticles into clusters. Each cluster consists of N spherical nanoparticles ($4 \leq N \leq 39$). The final configurations of clusters match well between simulations and experiments for the N explored experimentally by Manoharan *et al.* [12] ($N \leq 15$). For $N > 16$, the clusters are in unfamiliar packings. Many of them possess a high-symmetry point group. For all

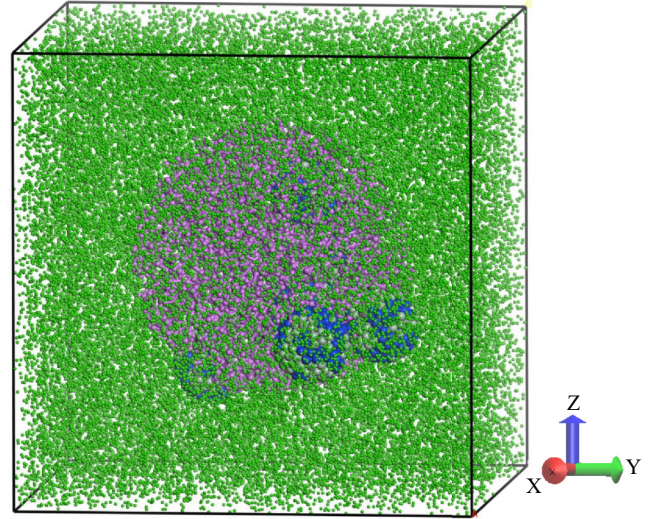


FIG. 1. Representative snapshot of one simulated system at the beginning of the simulation run. Green and purple beads represent water and oil, respectively. Under the condition of oil-in-water emulsions, oil beads form a large spherical droplet. Nanoparticles (NPs) are shown in smaller spheres, consisting of 96 polar beads (blue) and 96 nonpolar beads (gray). NPs are firmly attached to the droplet surface by the surface tension effect. For visual clarity, water beads are represented at a smaller scale compared to oil beads and apolar-polar beads.

N values, we observe a structural transition between spherical packings to M_2 or these unfamiliar packings. Also, the critical volume at which the structural transition occurs increases as a cubic function of the number of adsorbed particles.

II. MODEL AND METHOD

Figure 1 illustrates a typical initial configuration of the simulation system, consisting of mesomolecule models of water, oil (decane), and nanoparticles. The initial condition prohibits the presence of water particles within the oil droplets, ensuring a distinct phase separation between the two components. Fan and Striolo [31] used a degree of coarse-graining where one DPD bead is equivalent to five water molecules. Given that the volume of a water molecule at room temperature is 30 \AA^3 , the volume of a water bead (w) is 150 \AA^3 . At the standard density of three beads per cubic length scale, this translates to a fundamental length unit of $R_c = (3 \times 150 \text{ \AA}^3)^{1/3} = 7.66 \text{ \AA}$, which can be considered as the radius of all the DPD beads ($7.66 \text{ \AA}/2 = 3.83 \text{ \AA}$). Likewise, the mass of a water molecule is 18 amu, and therefore, the mass of a water bead is 90 amu.

In the coarse-graining approach in Refs. [31,32], the oil bead is intended to represent the decane. As the volume of each decane molecule is 323 \AA^3 , two oil beads (o) represent a single molecule of decane so that all DPD beads have the same volume. These two beads are coupled by a harmonic spring of length $0.72R_c$ and spring constant $350 k_B T/R_c$, where k_B is the Boltzmann constant and T is the absolute temperature of the system, in order to preserve the linear form of decane [31].

Each Janus nanoparticle is represented by a hollow rigid sphere with 192 beads on its surface. By setting the radius of

nanoparticles to $2R_c$, the NPs in the system have a reduced density of three beads per cubic length scale, similar to the reduced density of water. Such a number of beads on the NP surface is adequate to prevent any bead, whether water or decane, from unphysically penetrating the NP [31]. There are two types of nanoparticle (NP) beads: polar (p) and nonpolar (ap), which are distributed on the surface of the nanoparticle to form distinct regions. The term ‘‘Janus’’ NP was initially used to describe particles with inhomogeneous wettability, where the polar and apolar regions were equal in area. By adjusting the ratio between the number of apolar and polar beads, denoted by f , the apolar and polar area ratio can be varied. A higher f value leads to a larger apolar region, while a lower f value results in a larger polar region.

The equilibrium position of Janus NPs at the water-oil interface was analyzed in terms of two parameters: the ratio f and the contact angle between the NP and the interface. However, as the final assembled structures seem to be minimally affected by the contact angle [20], we consider only the ratio f in our analysis. Two NP types are simulated, all with radius $2R_c$: (1) NPs with 96 polar and 96 nonpolar beads ($f = 0.5$) and (2) NPs with 64 polar and 128 nonpolar beads ($f = 0.75$). To maintain the spherical morphology of the NP, all the beads on the NP are restrained to their center by a harmonic functional form of a few times $k_B T/R_c$ in the spring constant.

We carry out the DPD simulations using the Mesocite module from the Materials Studio package. The details of the DPD calculation can be found in the Appendix. The size of the cubic simulation box is $30 \times 30 \times 30R_c^3$ with periodic boundary conditions along all three directions. At the beginning of the simulations, the water beads are distributed randomly in the simulation box, and the oil beads form a spherical droplet of radius $12R_c$. A given number of NPs N ($N = 4$ to 39) is initially located randomly at the droplet surface.

As described in the Appendix, the pair interactions are represented by combining a dissipative force, random force, and conservative force. Among these, only the conservative force depends on the specific bead types involved in each pair. It is characterized as a soft repulsion and can be fully described by a single parameter, a_{ij} . Groot and Warren matched the water compressibility to determine the interaction parameter (a_{ii}) of water [33]. For one water bead of five molecules, a_{w-w} was found to be $131.5 k_B T/R_c$. Here we also assign $a_{w-w} = a_{o-o} = 131.5 k_B T/R_c$ because the pressure is constant and oil and water beads have the same volume. To simplify the parametric calculations, we employ $a_{p-p} = a_{ap-ap} = 450 k_B T/R_c$ [34,35].

As suggested by Fan and Striolo [31], the water-oil interaction parameter was parameterized to match the experimental water-decane interface tension ($\gamma = 51.7 \text{ mNm}^{-1}$) [36], yielding $a_{o-w} = 198.5 k_B T/R_c$. NP-solvent interaction parameters, including a_{o-p} , a_{o-ap} , a_{w-p} , and a_{w-ap} , were set similarly to those reported in Refs. [34,35]. In this procedure, the NP-solvent interaction parameters were determined to match three-phase contact angles obtained in molecular dynamics simulations for one silica NP at the decane-water interface [37]. The numerical values of all interaction parameters implemented in the simulations are given in Table I.

TABLE I. Interaction parameters a_{i-j} used in DPD simulations, expressed in $k_B T/R_c$ units, $1 k_B T/R_c = 0.08 \text{ kcal}/(\text{mol } \text{Å})$.

	w	o	ap	p
w	131.5	198.5	178.5	110
o		131.5	161.5	218.5
ap			131.5	670
p				450

Our model’s primary aim is to simulate a Pickering emulsion scenario. In such emulsions, when oil and water are mixed, they form small oil droplets that are dispersed throughout the water, creating an oil-in-water emulsion. Over time, these droplets will naturally coalesce to reduce the system’s overall energy. However, the addition of Janus nanoparticles to this mixture stabilizes the emulsion. These particles adhere to the oil-water interface, preventing the droplets from coalescing. Evaporation in experiments typically refers to the process of oil droplets dispersed in water transitioning to a gas state due to an increase in temperature or pressure drop [12,18]. In our simulations, the term ‘‘evaporation’’ refers to the process where the oil droplet is gradually removed from the system. This reduction is implemented by reducing the number of oil beads in our simulations at a steady rate. In addition, it is only the oil droplet that undergoes gradual evaporation, while the water does not evaporate. Furthermore, we are not explicitly addressing the diffusive nature of evaporation. This is a simplified representation, primarily meant to induce the assembly of Janus nanoparticles, rather than to capture the full complexity of real-world evaporation dynamics which would involve diffusion and other processes.

All mesoscopic DPD simulations are performed in the NVT ensemble. Each simulation runs a total 3×10^6 time steps. In order to mimic the low evaporation observed in experiments, we implement a sweep mechanism to control the evaporation rate. The evaporation amplitude, denoted as ΔR , is defined as the ratio between the initial radius of the nanoparticles and the number of sweeps. During each sweep, a specific number of oil beads belonging to the spherical shell is removed from the system. The number of oil beads removed can be calculated using the equation

$$\frac{4}{3}\pi\rho\{R(t)^3 - [R(t) - \Delta R]^3\}, \quad (1)$$

where $R(t)$ is the radius of the oil droplet at time t , and ρ is the number density of the oil beads. This mechanism leads to a slight decrease in the droplet radius. The removal of the oil beads continues until the droplet completely vanishes after 2×10^6 time steps, equivalent to 20 sweeps. Following this procedure, we have 10^6 time steps (10 sweeps) remaining to examine the stability of the clusters obtained against thermal fluctuation. In each sweep during evaporation, the polar, nonpolar beads, and NPs rearrange to a new equilibrium. This strategy replaces the evaporation dynamics with a set of equilibrium states [20].

For a given number of NPs N ($N = 4$ to 39), 15 simulations with different initial configurations are repeated to confirm the validity of the cluster structures and average the obtained data. In the DPD model, the beads do not represent real atoms

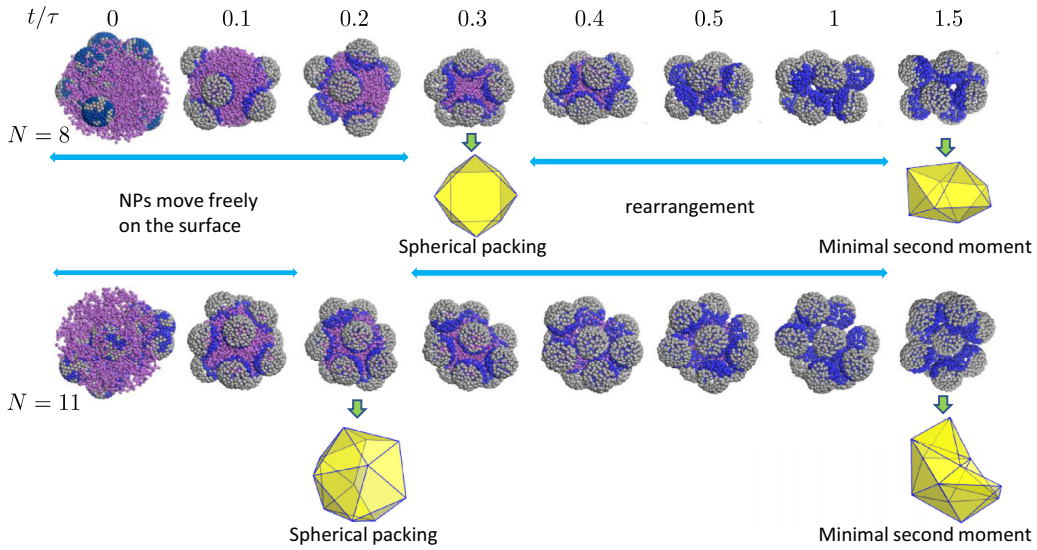


FIG. 2. Simulation snapshots for eight-sphere cluster (first row) and 11-sphere cluster (second row) taken during evaporation process of the oil droplet, displaying the evolution of the system between states. The water beads are not shown for clarity. NPs move freely over the droplet’s surface until additional oil evaporates; they close together, assembling in a spherical packing (illustrated by a yellow polyhedron). Further evaporation leads to a rearrangement of a cluster. The final structure of the two clusters that minimize the second moment is also shown. The snapshots are taken at various intervals of τ , where τ is the time when the droplet vanishes.

or molecules but, rather, small regions of fluid interacting via phenomenological forces. All beads have the same mass (m) and interaction radius (R_c), thus it is convenient to introduce a reduced system of units in which the bead mass and interaction radius are the units of mass and length. An additional reference quantity is needed, taken as energy scale (E_{ref}), which is usually taken as the thermal energy, $k_B T$, at room temperature. Hence, all properties in our model are reported in these reduced units m , R_c , and E_{ref} , or combinations thereof. For example, timescale is measured in units of $R_c \sqrt{m/E_{\text{ref}}}$. To relate our results to a specific physical system, one would need to substitute the values of m , R_c , and E_{ref} with the appropriate physical units. Here, if we take $m = 0.09 \text{ kg mol}^{-1}$, $E_{\text{ref}} = 0.59 \text{ kcal mol}^{-1}$, and $R_c = 7.66 \text{ \AA}$, a timescale in our model would correspond to 4.61 ps in the physical time.

A time step of 0.05 in reduced units, which is equivalent to 0.23 ps in physical time units, is used to update the bead positions and momenta. Therefore, considering that one simulation run consists of a total of 3×10^6 time steps, the combined time for both the evaporation process of the oil droplets and the subsequent examination of cluster stability against thermal fluctuations amounts to approximately 700 ns. In relation to the timescales of experiments, which typically span tens of minutes, the timescales in our DPD simulations are considerably shorter. This discrepancy in timescales is a common challenge encountered in many coarse-grained simulations. However, we do not anticipate this disparity to significantly impact the validity of our final results.

The dissipation strength γ [see Eq. (A5)] is set to 4.5. In reality, during the evaporation process, there might be local variations in the fluid flow around the evaporating droplet due to factors such as temperature gradients, which can result in shearlike effects. By applying a shear force in our simulations, we attempted to take these complex, real-world interactions

into account, thereby making our model more robust and representative of the actual process. A shear force with a rate of 0.1 (in reduced units), applied in the y direction and in the yz shear plane, was determined based on preliminary simulations to ensure that it allows the oil droplet to deform but does not cause it to break apart, which would not be representative of the actual process we aim to model. This shear force is applied only until the oil droplet reaches a quasistable state and is then removed for the remainder of the simulation, allowing the Janus nanoparticles to assemble under the influence of evaporation alone.

III. RESULTS AND DISCUSSION

Figure 2 displays typical snapshots at different times of DPD simulations for $N = 8$ and $N = 11$. The initial configuration at $t = 0$ is a droplet formed by the oil beads and NPs trapped at its surface. For $N = 8$, at times $t/\tau = 0.1$, $t/\tau = 0.2$, where τ is the time at which the droplet is vanished completely, NPs move freely on the droplet surface. Until the droplet size is reduced to a critical value, i.e., at time $t/\tau = 0.3$, eight NPs, each of which acts as a point, are arranged in a regular square antiprism. Note that the square antiprism, where two square planes are parallel to each other but the rotated angle from each other is 45° , is a structure belonging to spherical packings (or spherical codes). Further shrinkage of the droplet then pushed NPs inward, leading to a rearrangement to a cluster. The configuration of this eight-sphere cluster at $t/\tau = 1$ is a snub disphenoid that minimizes the second moment of the mass distribution (called the minimal second moment) (see Supplemental Movie 1 in the Supplemental Material [38]).

Note also that our intent with continuing the simulation beyond τ (for instance, at $t/\tau = 1.5$) is to investigate any potential changes in the final structure of these clusters when

comparing the scenarios at $t/\tau = 1.0$ and at $t/\tau = 1.5$. After the characteristic drying time (τ), nanoparticles in such systems can experience rearrangement, a phenomenon attributed to several inherent features of the DPD model. The conservative forces acting between particles, which are crucial for structural formation, can induce rearrangements due to the balancing of these forces. In addition, the continuous interplay between dissipative and random forces, mimicking the effects of thermal fluctuations and Brownian motion, can also lead to rearrangements even after reaching equilibrium. The nature of DPD simulations, where particles interact with their neighbors, further allows changes in the local environment to cause rearrangements. Residual interactions between nanoparticles within a cluster, and time step sensitivity in the simulation can also contribute to such rearrangements.

Despite these factors leading to minor nanoparticle rearrangement, our findings do not reveal any significant alteration in the overall structure of the clusters. These rearrangements do not impact the overall cluster integrity and are not substantial enough to discern a difference between the cluster structures at $t/\tau = 1.0$ and $t/\tau = 1.5$. The minor rearrangements observed in our DPD simulations are indicative of the system's dynamic nature, even in the absence of the oil droplet.

Similarly, the 11-sphere cluster also undergoes a striking structural change upon evaporation, from spherical packing to the minimal second-moment configuration. The $N = 11$ cluster has a striking feature, as it is the lowest- N cluster with a nonconvex configuration.

Figure 3 compares the different cluster configurations obtained in the final stage of the simulation runs with those observed via experimental data [12]. Assembled clusters with varying numbers of NPs and coverage fractions f are shown. Apparently, the geometry of one given cluster depends only on the number N of particles that it contains, not on the coverage fraction. We find that for $N \leq 6$ the clusters have a triplet ($N = 3$) (not shown), tetrahedron ($n = 4$), triangular bipyramid ($N = 5$), and octahedron ($N = 6$). These clusters have the same configurations as spherical packings [19], Thomson structures [39], and Lennard-Jones structures [40], suggesting that small N -sphere cluster structures are insensitive to the optimal problems. For larger N , the configuration of the snub disphenoid is observed for $N = 8$, the triaugmented triangular prism for $N = 9$, the gyroelongated square bipyramid for $N = 10$, the nonconvex polyhedron for $N = 11$, and the icosahedron for $N = 12$. In particular, we monitored the NP, which is internal to the 11-sphere cluster configuration, and realized that it is positioned by six other neighboring NPs (maximum coordination number). The strongly repulsive force of the surrounding NPs makes it the weakest spot in the clusters under a force toward the center of the droplet. A common feature of all the clusters with $N \leq 11$ is that their packings follow the minimal second-moment distribution.

For $N \geq 12$, the clusters observed in the simulation runs and experiments differ from the minimal second-moment rule, but they lower their second moment during the packing process. For instance, for $N = 12$, we find the icosahedron, which is not a member of the minimal moment structures. We suppose that because all NPs positions are equivalent to each other in icosahedral symmetry, there is no weak position as

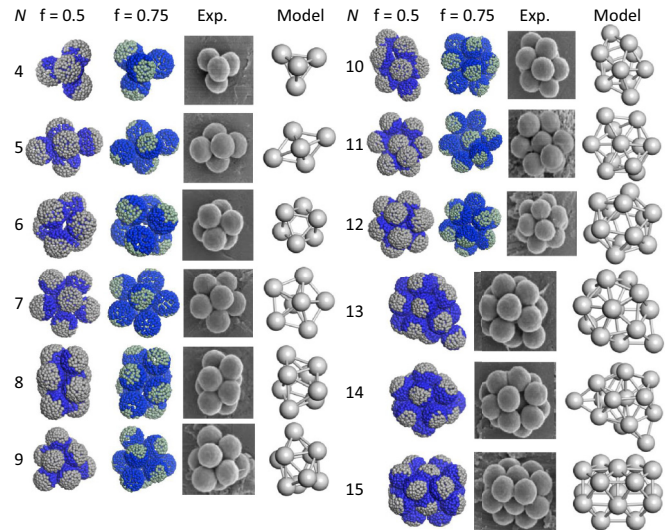


FIG. 3. Cluster structures corresponding at each N . At $N \leq 12$, the two first columns show the cluster structure as obtained by DPD simulations at $f = 0.5$ and $f = 0.75$, respectively. For comparison purposes, the third column is an electron micrograph of the clusters from the experiment of Manoharan *et al.* [12]. Adapted with permission from Ref. [12]. For $N > 12$, only clusters with $f = 0.75$ are shown. The right columns are corresponding model illustrations. For greater clarity, the spheres have been reduced in size, and the spheres have been connected by bonds. We consider a bond between two spheres when their center-to-center distance is smaller than $1.3\sigma_{\text{NP}}$, where σ_{NP} is the diameter of NPs.

the droplet collapses. The arrangement of spheres into small clusters can yield a diverse array of structures, especially when considering finite packings. The mathematical “kissing problem” [41] exemplifies this: while the surface of a central sphere can theoretically accommodate nearly 15 spheres, in practice only 12 spheres fit, leaving a significant amount of coordination area unused. These 12 spheres can adopt numerous configurations, including the highly symmetrical icosahedral packing and the less symmetrical “weary icosahedron.” In the case of our 13-sphere clusters, we observed “weary icosahedron” structures, which might be considered suboptimal in terms of symmetry. However, when additional constraints or conditions are in play, such as pairwise attractive forces, different structures can become more favorable. For instance, with a Lennard-Jones 6–12 potential, an icosahedron configuration is the most stable [42]. The “weary icosahedron” structures for $N = 13$ can be understood in the context of reducing the second moment of the mass distribution. This configuration results from the vertices of a regular icosahedron rolling down towards the south pole until reaching an equilibrium position [19,43]. The 14-sphere cluster is obtained by adding one sphere to one of the faces of the 13-sphere cluster. The cluster containing 15 spheres is a high-symmetry (D_{3h} group point) structure formed by two nine-sphere clusters (triaugmented triangular prism) sharing a face. For $N \leq 15$, our approach reproduces precisely all of the configurations examined in the experiment by Manoharan *et al.* [12], overcoming the limitations of the model given by Laura *et al.* [20], Peng *et al.* [23], and Schwarz *et al.* [18].

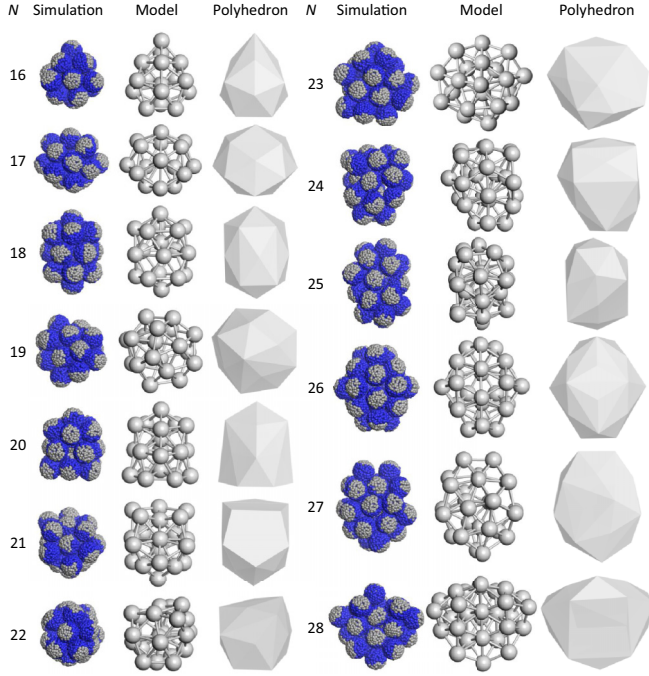


FIG. 4. Same as Fig. 3 but for $N = 16$ – 28 and $f = 0.75$. Right columns illustrate the polyhedra.

After having shown the reliability of our model, we study the structure of higher-order clusters. In Figs. 4 and 5, for $N = 16$, the cluster has a mirror plane that includes the north-south axis through the internal sphere (C_s point group). The 17-sphere cluster is a snub square antiprism (D_{4d} point-group symmetry) in addition to one internal sphere. It is one of the Johnson solids (J_{85}) that can be constructed as a square gyrobicupolae, connecting two anticupolae with gyrated orientations. The 17-sphere cluster was observed in the coordination polyhedron of NaHg_{16} [44]. For $N = 18$, we refer to the structure as “double icosahedra,” which is built from two complete icosahedra joined at an internal pentagonal face. It can also be considered as two gyroelongated pentagonal pyramids joined at the pentagonal face. This structure possesses the high-symmetry point group C_{5v} . It is also the lowest- N cluster that contains two interior spheres. Notable high symmetries are observed for $N = 21, 26, 31, 35$ and 38 , while lack of symmetry for $N = 19, 22, 23, 24, 28, 29, 30, 32, 33, 36, 37$. At $N = 38$, the structure is a truncated octahedron with O_h symmetry group. Its surface has eight hexagonal close-packed and six square facets (see Supplemental Movie 2 [38]). Interestingly, the global minimum for the Lennard-Jones [42], Pacheco and Prates-Ramalho [45], and Girifalco potentials [46] at $N = 38$ is also the truncated octahedron. Finally, we give a brief comparison with the optimal spherical packings. For $N \leq 7$, these clusters are essentially the same as ours. The clusters are quite different for $N > 7$, except for $N = 12$. While all the M_2 -minimal packings at $N \leq 11$ are identical to those. A typical characteristic of high-order clusters is that interpenetrating motifs of slightly distorted pentagonal, hexagonal, or icosahedral symmetry may be recognized.

In the last step of simulations, when cluster configurations have reached a stable state, the component NPs align so that

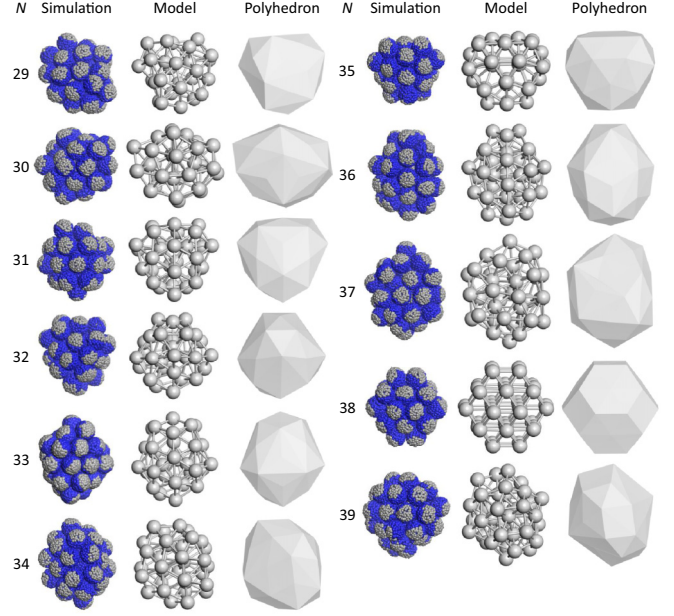


FIG. 5. Same as Fig. 3 but for $N = 29$ – 39 .

their apolar beads face each other to decrease the total potential energy. Utilizing an orientational order parameter [47],

$$P = \left\langle \frac{1}{N} \sum_{i=1}^N \mathbf{n}_i \cdot \frac{\mathbf{r}_{\text{cm}} - \mathbf{r}_i}{|\mathbf{r}_{\text{cm}} - \mathbf{r}_i|} \right\rangle, \quad (2)$$

where \mathbf{r}_i is the center of mass of i th NP, \mathbf{r}_{cm} is the center of mass of the cluster, and \mathbf{n}_i is the unit vector pointing in the direction of apolar beads of NP i th. The angular brackets represent an average across all simulation runs that are made up of N NPs. For an utterly spherical cluster where all NPs directional vectors point toward the cluster’s center, $P = 1$ holds. If $P \geq 0.9$, we regard clusters as spherical (denoted as S). Otherwise, we consider any cluster with $0.5 \leq P < 0.9$ nonspherical and label it NS. Finally, $P < 0.5$ clusters are regarded to have randomly oriented.

In Fig. 6 we plot two of the most representative geometrical properties for the clusters shown in Figs. 3–5: the orientational order parameter and the average coordination number. Notice that all the clusters with $N \leq 15$, except for $N = 14$, belong to the spherical cluster, while the clusters with $15 \leq N \leq 39$ are nonspherical, and none of them is randomly oriented. This is intuitively reasonable since high-order clusters generally have less symmetry and contain interior spheres that reduce the orientational order parameter. The spherical and nonspherical clusters are fascinating micelles [48]. The average coordination number, \bar{N}_b , increases quickly with an increase of N for the spherical clusters but increases slowly in the nonspherical clusters. The average coordination number is in the range of 3.1–3.7 at $N > 15$. Table II summarizes the results on the geometrical properties of all the clusters obtained by the DPD simulations. Numerical coordinates for all these clusters are included in the Supplemental Material [38].

Our findings also confirm the experimental observation of Manoharan *et al.* [12] and simulations of Lauga *et al.* [20] that because every N -particle droplet system undergoes a

TABLE II. Total number of bonds, average bond number, symmetry, and cluster type classified based on the orientational bond order P for the structures from $N = 4$ to 39.

N	N_b	\bar{N}_b	Schoenflies point group	P	N	N_b	\bar{N}_b	Schoenflies point group	P	N	N_b	\bar{N}_b	Schoenflies point group	P
4	6	1.5	T_d	S	16	48	3	C_s	NS	28	97	3.46	C_1	NS
5	9	1.8	D_{3h}	S	17	48	2.82	D_{4d}	NS	29	98	3.38	C_1	NS
6	12	2	O_h	S	18	56	3.11	C_{5v}	NS	30	107	3.57	C_1	NS
7	16	2.28	D_{5h}	S	19	58	3.05	C_1	NS	31	106	3.42	C_3	NS
8	18	2.25	D_{2d}	S	20	65	3.25	C_s	NS	32	110	3.43	C_1	NS
9	21	2.33	D_{3h}	S	21	74	3.52	C_{2v}	NS	33	114	3.45	C_1	NS
10	24	2.4	D_{4d}	S	22	74	3.36	C_1	NS	34	121	3.58	C_2	NS
11	31	2.81	C_{2v}	S	23	76	3.30	C_1	NS	35	127	3.63	C_{2v}	NS
12	30	2.5	I_h	S	24	82	3.41	C_1	NS	36	128	3.55	C_1	NS
13	38	2.92	C_s	S	25	87	3.48	C_s	NS	37	135	3.65	C_1	NS
14	41	2.92	C_1	NS	26	85	3.27	D_{3h}	NS	38	144	3.79	O_h	NS
15	42	2.8	D_{3h}	S	27	91	3.37	C_2	NS	39	144	3.69	C_1	NS

spherical packing, each N -sphere cluster looks precisely the same. We observe that this remark also holds as $15 < N \leq 39$. The initial spherical packing is unique for the regime we investigate, and the subsequent evolution of the NPs is so highly restrained that only one resulting packing is compatible with the restraint. The final configurations observed are independent of the coverage fraction and the initial state of the nanoparticles on the droplet surface. If the evaporation process proceeds slowly enough, the NPs should be arranged in spherical packing to maximize the distance between the nearest pair of points. To verify this hypothesis, we calculated the cosine of the minimal angular distance θ_{\min} (i.e., the inner product of the closest points) as a function of time. The $\cos \theta_{\min}$ function [Fig. 7(a)] shows a decrease in time and achieves constant values at certain times depending on the number of constituent nanoparticles. In particular, for $N = 7, 8, 10$, and 11 , the curves have a minimum, while for $N = 4, 5, 6$, and 9 , they evolve smoothly without a minimum point. Note that in the clusters with $4, 5, 6$ and 9 spheres, the optimal structure for both the spherical packing and minimal-

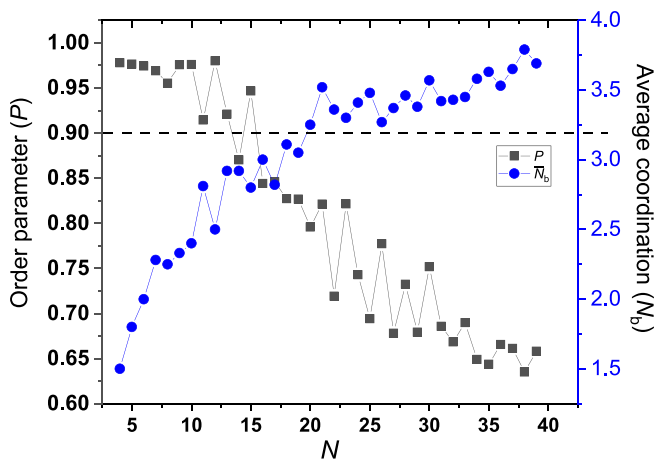


FIG. 6. Structural properties as a function of the cluster size. The black line is the orientational order parameter, and the blue line is the average coordination. The dashed line indicate the criteria to distinguish between the spherical cluster and nonspherical cluster.

moment packing is the same. However, for $N = 7, 8, 10$, and 11 , their optimal structures for both packings are different. Therefore, the minimum point in the cosine of the minimal angular distance (denoted by an asterisk) can be used as a useful parameter to detect the transition time between the two packings. For $N > 12$ where the minimal-moment rule may no longer hold, but they lower their second moment during the packing process [Fig. 7(b)], whenever the minimum point appears, the structural transition should occur. Numerical evolution of the θ_{\min} and the second moment M_2 as a function of time settles down to a steady value, indicating stable packings of clusters. We determine the critical volume V_C of the oil droplet at which the structural transition from the spherical packing (SP) to the minimal second packings (M_2) and/or (U) packing. In Fig. 8 the two-structure regions are clear for $N \leq 6$ and $N = 9$, and the SP- M_2 structure separation region is found at $N = 7, 8, 10$, and 11 . The optimal physical quantity underlying the observations remains unknown for $N > 13$, which is denoted as the undefined U structure. Figure 8 shows that V_C/V_{NP} , where V_{NP} is the volume of one nanoparticle, increases as a function of the number of NPs on the droplet. A mathematical function fitted to the observation is given by the equation $V_C/V_{NP} = 1.2333 + 0.6166N + 0.1028N^2 + 0.0057N^3$ with R^2 of 0.999. The coefficients of the third-order polynomial depend on the nearest neighboring distance between the NPs. As a consequence, they can be controlled by tuning interparticle interaction parameters a_{i-i} or the ratio between the number of nonpolar and polar beads in the nanoparticle.

IV. CONCLUSIONS

In conclusion, we have performed a dissipative particle dynamics simulation to investigate the structure assembled by nanoparticles restricted to the interface of oil emulsion droplets distributed in an aqueous phase during evaporation. The simulation approach accurately reproduces the structures of N -sphere clusters compared to those obtained experimentally ($N \leq 15$). It also confirmed the experimental observation of Manoharan *et al.* [12] and several experimental studies reported in the literature that each N -sphere cluster is identical

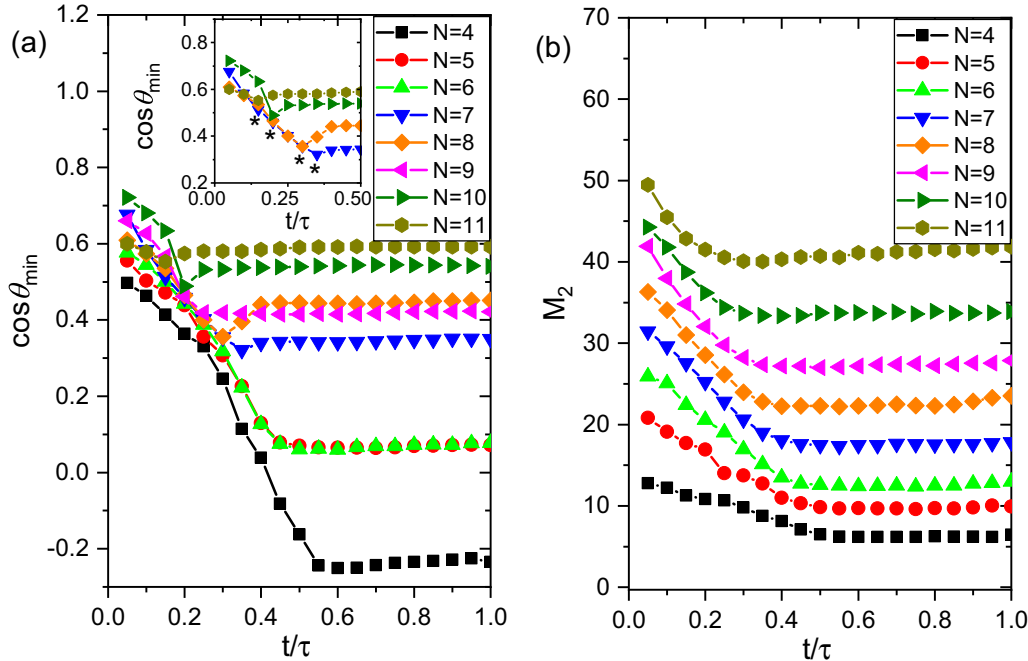


FIG. 7. (a) Cosine of the minimal angular distance of different N -sphere clusters and (b) the second moment of the mass distribution as a function of time.

because each N -particle cluster must go through an optimal spherical packing, regardless of the initial distribution of NPs on the droplet. We observe that this remark also holds as $15 < N \leq 39$. Many cluster structures have interesting high symmetry, e.g., $N = 17, 18, 26, 35, 38$ that are possibly members of a set of magic numbers known from in atomic scales [49].

We have calculated the minimal angular distance between the nearest pair of nanoparticles and found that it can be used as an indicator to distinguish the structural transition between the spherical packings to the M_2 -minimal packings.

Although for $N > 12$ the cluster structures no longer obey the M_2 -minimal rule, those structures lower their second moment. Finally, the critical volume at which the structural transition occurs is determined to be a cubic function of the number of constituent nanoparticles. While a number of effects, such as the effect of the evaporation rate and self-self interaction parameters, are certainly not included in our model, the molecular insights provide a tentative anticipation of clusters with precisely defined structures. Future work could be directed towards a larger number of spheres to determine whether the phenomena of magic numbers commonly known in atomic clusters may extend to the domain of colloids.

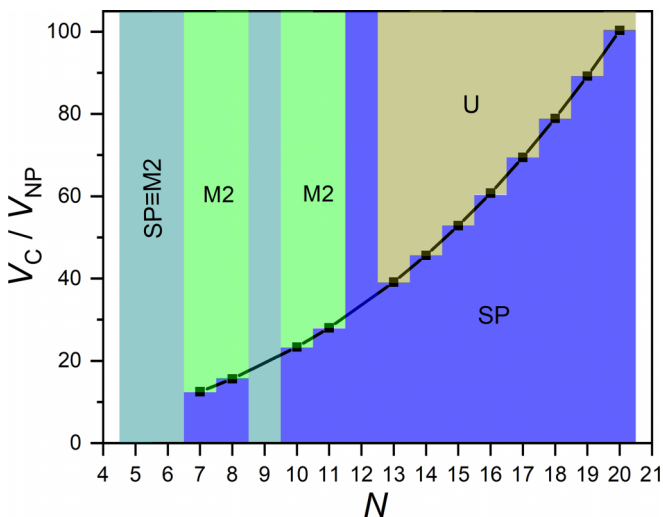


FIG. 8. Critical volume V_C depends upon the number of NPs (in units of the NP volume V_{NP}). The regions corresponding to different optimal pickings are colored accordingly. The line represents the best fit to the data.

ACKNOWLEDGMENT

This work was funded by the Ministry of Education and Training of Vietnam (MOET) under Grant No. B2021-SPH-11.

APPENDIX: THE DPD SIMULATION METHOD

DPD represents a dynamic particle simulation method [33,50]. It involves the calculation of particle movement by solving the corresponding equations of motion over a specific time duration. These equations delineate the behavior of particles under the influence of various forces. The distinctive feature of DPD is the simulation of particle motion at a constant temperature, with the forces encompassing those from a unique thermostat. DPD employs a momentum-conserving and stochastic thermostat, which sets it apart from Brownian or molecular dynamics.

Let's consider an assembly of interacting beads, each with a uniform mass m . If we denote the position of bead i as \mathbf{r}_i and its velocity as \mathbf{v}_i , the changes in these parameters over time are

described by the motion equations

$$\frac{\partial \mathbf{r}_i}{\partial t} = \mathbf{v}_i, \quad \frac{\partial \mathbf{v}_i}{\partial t} = \frac{\mathbf{f}_i}{m}, \quad (\text{A1})$$

where \mathbf{f}_i represents the force exerted on bead i , which originates from its interaction with the remaining beads. Generally, this force can be expressed as

$$\mathbf{f}_i = \sum_{i \neq j} (\mathbf{F}_{ij}^{\text{C}} + \mathbf{F}_{ij}^{\text{D}} + \mathbf{F}_{ij}^{\text{R}}), \quad (\text{A2})$$

where the sum runs over all other particles within a specified cutoff radius R_c . The term enclosed within the brackets constitutes the force that results from the interaction of bead i with its neighboring bead j , regardless of whether they are bonded or not. This force component comprises three parts: conservative (C), dissipative (D), and random (R).

The conservative, dissipative, and random forces all exhibit a shared structure.

$$\mathbf{F}_{ij} = C_{ij} \omega(r_{ij}) \mathbf{e}_{ij}, \quad (\text{A3})$$

where $C_{ij} (= C_{ji})$ represents a symmetric force amplitude and r_{ij} denotes the distance between particles i and j , while \mathbf{e}_{ij} is the unit vector $(\mathbf{r}_i - \mathbf{r}_j)/r_{ij}$. The radial dependence of the force is determined by the function $\omega(r)$, which is continuous and positive for $r < R_c$, turning zero for $r \geq R_c$. This function serves to distribute the force amplitude C across an interaction shell with radius R_c . The force proves to be repulsive when $C_{ij} > 0$ and attractive when $C_{ij} < 0$. From Eq. (A3), it follows that the forces conform to Newton's third law, i.e., $\mathbf{F}_{ij} = -\mathbf{F}_{ji}$. Therefore, these forces do not contribute to the total force exerted on the system. Given that the total force is zero, the total momentum remains constant throughout the motion, a necessary condition for simulating hydrodynamics.

The conservative force, \mathbf{F}^{C} , is calculated as

$$\mathbf{F}_{ij}^{\text{C}} = a_{ij} \omega^{\text{C}}(r_{ij}) \mathbf{e}_{ij}, \quad (\text{A4})$$

where $a_{ij} = a_{ji} > 0$, suggesting that the force is invariably repulsive. For the conservative force, DPD implements a straightforward linear weight function, expressed as $\omega^{\text{C}}(r) = 1 - r/R_c$ for $r < R_c$.

The dissipative force, \mathbf{F}^{D} , is directly proportional to the rate at which two beads are moving towards each other, given by

$$\mathbf{F}_{ij}^{\text{D}} = -\gamma_{ij} \omega^{\text{D}}(r_{ij}) (\mathbf{v}_{ij} \cdot \mathbf{e}_{ij}) \mathbf{e}_{ij}, \quad (\text{A5})$$

where $\gamma_{ij} = \gamma_{ji} > 0$ and $\mathbf{v}_{ij} = \mathbf{v}_i - \mathbf{v}_j$. The central component, $(\mathbf{v}_{ij} \cdot \mathbf{e}_{ij})$, is positive when two beads are moving towards each other, giving rise to a repulsive dissipative force.

Conversely, if the two beads are moving apart, the central component turns negative, resulting in an attractive dissipative force. As such, the dissipative force always operates to reduce the relative central velocity. DPD utilizes a quadratic function to represent the dissipative force, which is given by $\omega^{\text{D}}(r) = (1 - r/R_c)^2$ when $r < R_c$.

The random force, \mathbf{F}^{R} , interacts between pairs of beads

$$\mathbf{F}_{ij}^{\text{R}} = \sigma_{ij} \omega^{\text{R}}(r_{ij}) \xi_{ij} \frac{1}{\sqrt{\Delta t}} \mathbf{e}_{ij}, \quad (\text{A6})$$

where $\sigma_{ij} = \sigma_{ji} > 0$, and Δt represents the time step utilized in solving the equations of motion [Eq. (A1)]. In the context of DPD, a linear weight function is used for the random force, which is formulated as $\omega^{\text{R}} = 1 - r/R_c$ for $r < R_c$. The term $\xi_{ij} = \xi_{ji}$ is a random number characterized by a zero mean and unit variance,

$$\langle \xi_{ij} \rangle = 0, \quad \langle \xi_{ij}^2 \rangle = 1. \quad (\text{A7})$$

For simplicity's sake, DPD utilizes a uniform distribution, where a random number is independently drawn for each interacting pair at every time step. Given that ξ_{ij} can be either positive or negative, the random force can be either repulsive or attractive.

The fluctuation-dissipation theorem [51] provides the relationship between the parameters of the random force (σ_{ij} and ω^{R}), the dissipative force (γ_{ij} and ω^{D}), and the temperature T ,

$$\omega^{\text{R}}(r) = \sqrt{\omega^{\text{D}}(r)}, \quad \sigma_{ij} = \sqrt{\gamma_{ij} 2k_B T}, \quad (\text{A8})$$

where k_B is Boltzmann's constant.

The positions and velocities of the beads are computed using a modified velocity-Verlet algorithm, which was initially proposed by Groot and Warren [33],

$$\begin{aligned} \mathbf{r}_i(t + \Delta t) &= \mathbf{r}_i(t) + \Delta t \mathbf{v}_i(t) + \frac{1}{2} (\Delta t)^2 \mathbf{f}_i(t), \\ \tilde{\mathbf{v}}_i(t + \Delta t) &= \mathbf{v}_i(t) + \lambda \Delta t \mathbf{f}_i(t), \\ \mathbf{f}_i(t + \Delta t) &= \mathbf{f}_i(\mathbf{r}(t + \Delta t), \tilde{\mathbf{v}}_i(t + \Delta t)), \\ \mathbf{v}_i(t + \Delta t) &= \mathbf{v}_i(t) + \frac{1}{2} \Delta t (\mathbf{f}_i(t) + \mathbf{f}_i(t + \Delta t)). \end{aligned} \quad (\text{A9})$$

In the case where the force is not influenced by velocity, one would obtain the original velocity-Verlet algorithm for $\lambda = 1/2$. However, because the force does depend on velocity, we need to make a prediction for the new velocity, denoted as $\tilde{\mathbf{v}}$, and subsequently correct it in the final step. This advanced algorithm still updates the force once per iteration, specifically after the second step, ensuring minimal increase in computational cost.

-
- [1] M. A. Boles, M. Engel, and D. V. Talapin, *Chem. Rev.* **116**, 11220 (2016).
 [2] S. A. Mallory, C. Valeriani, and A. Cacciuto, *Annu. Rev. Phys. Chem.* **69**, 59 (2018).
 [3] C. Zong, *Sphere Packings* (Springer Science & Business Media, New York, 2008).
 [4] H. P. Van, A. Fortini, and M. Schmidt, *Phys. Rev. E* **101**, 012608 (2020).
 [5] F. Li, D. P. Josephson, and A. Stein, *Angew. Chem., Int. Ed.* **50**, 360 (2011).
 [6] H. Pham Van, A. Fortini, and M. Schmidt, *Phys. Rev. E* **93**, 052609 (2016).
 [7] S. Park, H. Hwang, M. Kim, J. H. Moon, and S.-H. Kim, *Nanoscale* **12**, 18576 (2020).
 [8] C. S. Plüsch and A. Wittmann, *Macromol. Rapid Commun.* **34**, 1798 (2013).
 [9] B. Binks and P. Fletcher, *Langmuir* **17**, 4708 (2001).
 [10] O. D. Velev, K. Furusawa, and K. Nagayama, *Langmuir* **12**, 2374 (1996).

- [11] J. Wang, C. F. Mbah, T. Przybilla, B. Apeleo Zubiri, E. Spiecker, M. Engel, and N. Vogel, *Nat. Commun.* **9**, 5259 (2018).
- [12] V. N. Manoharan, M. T. Elsesser, and D. J. Pine, *Science* **301**, 483 (2003).
- [13] G.-R. Yi, V. N. Manoharan, E. Michel, M. T. Elsesser, S.-M. Yang, and D. J. Pine, *Adv. Mater.* **16**, 1204 (2004).
- [14] Y.-S. Cho, G.-R. Yi, S.-H. Kim, D. J. Pine, and S.-M. Yang, *Chem. Mater.* **17**, 5006 (2005).
- [15] C. S. Wagner, Y. Lu, and A. Wittemann, *Langmuir* **24**, 12126 (2008).
- [16] M. Hoffmann, C. S. Wagner, L. Harnau, and A. Wittemann, *ACS Nano* **3**, 3326 (2009).
- [17] C. S. Wagner, B. Fischer, M. May, and A. Wittemann, *Colloid Polym. Sci.* **288**, 487 (2010).
- [18] I. Schwarz, A. Fortini, C. S. Wagner, A. Wittemann, and M. Schmidt, *J. Chem. Phys.* **135**, 244501 (2011).
- [19] N. J. A. Sloane, R. H. Hardin, T. D. S. Duff, and J. H. Conway, *Discrete Comput. Geom.* **14**, 237 (1995).
- [20] E. Lauga and M. P. Brenner, *Phys. Rev. Lett.* **93**, 238301 (2004).
- [21] N. J. A. Sloane, R. H. Hardin, W. D. Smith *et al.*, <http://neilsloane.com/packings/> (2000).
- [22] D. Kottwitz, *Acta Cryst. A* **47**, 158 (1991).
- [23] B. Peng, F. Smalenburg, A. Imhof, M. Dijkstra, and A. van Blaaderen, *Angew. Chem.* **125**, 6841 (2013).
- [24] F. Sciortino, A. Giacometti, and G. Pastore, *Phys. Rev. Lett.* **103**, 237801 (2009).
- [25] Z.-W. Li, Z.-Y. Lu, Z.-Y. Sun, and L.-J. An, *Soft Matter* **8**, 6693 (2012).
- [26] E. Bianchi, A. Z. Panagiotopoulos, and A. Nikoubashman, *Soft Matter* **11**, 3767 (2015).
- [27] Y. Kobayashi, N. Arai, and A. Nikoubashman, *Soft Matter* **16**, 476 (2020).
- [28] F. Sciortino, A. Giacometti, and G. Pastore, *Phys. Chem. Chem. Phys.* **12**, 11869 (2010).
- [29] R. Fantoni, A. Giacometti, F. Sciortino, and G. Pastore, *Soft Matter* **7**, 2419 (2011).
- [30] G. Rosenthal, K. E. Gubbins, and S. H. Klapp, *J. Chem. Phys.* **136**, 174901 (2012).
- [31] H. Fan and A. Striolo, *Phys. Rev. E* **86**, 051610 (2012).
- [32] H. Fan and A. Striolo, *Soft Matter* **8**, 9533 (2012).
- [33] R. D. Groot and P. B. Warren, *J. Chem. Phys.* **107**, 4423 (1997).
- [34] X.-C. Luu, J. Yu, and A. Striolo, *Langmuir* **29**, 7221 (2013).
- [35] X.-C. Luu, J. Yu, and A. Striolo, *J. Phys. Chem. B* **117**, 13922 (2013).
- [36] A. Goebel and K. Lunkenheimer, *Langmuir* **13**, 369 (1997).
- [37] H. Fan, D. E. Resasco, and A. Striolo, *Langmuir* **27**, 5264 (2011).
- [38] See Supplemental Material at <http://link.aps.org/supplemental/10.1103/PhysRevE.108.014602> for the dynamic process of cluster formation and the numerical coordinates of all clusters within the range of N values from 4 to 39.
- [39] M. Atiyah and P. Sutcliffe, *Milan J. Math.* **71**, 33 (2003).
- [40] M. Hoare and P. Pal, *Adv. Phys.* **20**, 161 (1971).
- [41] J. H. Conway and N. J. A. Sloane, *Sphere Packings, Lattices and Groups*, Grundlehren der mathematischen Wissenschaften, Vol. 290 (Springer Science & Business Media, New York, 2013).
- [42] D. J. Wales and J. P. Doye, *J. Phys. Chem. A* **101**, 5111 (1997).
- [43] V. N. Manoharan and D. J. Pine, *MRS Bull.* **29**, 91 (2004).
- [44] T. Hohl, F. Tambornino, and C. Hoch, *Crystals* **12**, 1679 (2022).
- [45] J. M. Pacheco and J. P. Prates Ramalho, *Phys. Rev. Lett.* **79**, 3873 (1997).
- [46] L. A. Girifalco, *J. Phys. Chem.* **96**, 858 (1992).
- [47] S. Whitelam and S. A. Bon, *J. Chem. Phys.* **132**, 074901 (2010).
- [48] A. Jackson-Davis, S. White, L. Kassama, S. Coleman, A. Shaw, A. Mendonca, B. Cooper, E. Thomas-Popo, K. Gordon, and L. London, *J. Food Protect.* **86**, 100025 (2023).
- [49] F. Baletto and R. Ferrando, *Rev. Mod. Phys.* **77**, 371 (2005).
- [50] E. Moeendarbary, T. Y. Ng, and M. Zangeneh, *Int. J. Appl. Mech.* **01**, 737 (2009).
- [51] P. Espanol and P. Warren, *Europhys. Lett.* **30**, 191 (1995).